

## Rapid TiO<sub>2</sub>/SBA-15 synthesis from ilmenite and use in photocatalytic degradation of dimethoate under simulated solar light

Ge Li<sup>a,b</sup>, Baodong Wang<sup>a,\*</sup>, Wayne Qiang Xu<sup>a,\*\*</sup>, Yifan Han<sup>b</sup>, Qi Sun<sup>a,\*\*\*</sup>

<sup>a</sup> National Institute of Clean-and-Low-Carbon Energy, Beijing 102211, China

<sup>b</sup> State Key Laboratory of Chemical Engineering, East China University of Science and Technology, Shanghai 200237, China



### ARTICLE INFO

#### Keywords:

TiO<sub>2</sub>/SBA-15  
Ilmenite  
Photocatalysis  
Simulated solar light  
Dimethoate

### ABSTRACT

SBA-15 mesoporous materials loaded with 8%–42% TiO<sub>2</sub> were prepared by post-synthesis hydrolysis using ilmenite as the TiO<sub>2</sub> source. X-ray diffraction, high-resolution transmission electron microscopy, nitrogen adsorption–desorption measurements, and Fourier-transform infrared, X-ray photoelectron, Raman, and ultra-violet-visible spectroscopies were used to investigate the TiO<sub>2</sub>/SBA-15 morphology and crystal structure. The results show that TiO<sub>2</sub> was successfully loaded on the mesoporous SBA-15 and the highly ordered two-dimensional hexagonal structure was stable. The photocatalytic performances of the samples in dimethoate degradation under simulated solar light were investigated. The photocatalytic activity initially increased and then decreased with increasing TiO<sub>2</sub> loading. The 26% TiO<sub>2</sub>/SBA-15 sample showed the highest photocatalytic activity and completely degraded dimethoate within 7 h. The catalytic activity of TiO<sub>2</sub>/SBA-15 was 62% higher than that of pure TiO<sub>2</sub>. This may be because of a synergistic effect resulting from the adsorption of dimethoate on the mesoporous material. The presence of Ti–O–Si species enhances the TiO<sub>2</sub> surface acidity and formation of surface adsorption sites; The adsorption and electron delocalization properties of SBA-15 are the main reasons for the observed enhancement of the pesticide degradation rate. These improves the TiO<sub>2</sub>/SBA-15 photocatalytic activity. TiO<sub>2</sub>/SBA-15 maintained high photocatalytic activity and good stability during four cycles, with a dimethoate degradation rate greater than 94%. The byproducts generated during photocatalysis were identified using gas chromatography-mass spectrometry. The photocatalytic degradation of dimethoate followed first-order kinetics. The mechanism of the photocatalytic degradation of dimethoate was investigated.

### 1. Introduction

The extensive use of organophosphorus pesticides enables increased agricultural production, but the widespread use of pesticides is also one of the main causes of environmental pollution. Pesticides affect the soil, water, air, plants, and other systems in the spraying area. They can also affect humans directly, and cause pollution and other hazards. Organophosphorus pesticides are highly toxic to humans and animals, and careless use and storage can result in poisoning. Low doses of dimethoate, which is an organophosphorus pesticide, has many chronic adverse effects on the human body, e.g., it is carcinogenic, teratogenic, and mutagenic, and causes nervous system disorders. It can also cause imposex. Dimethoate is resistant to photodegradation, relatively stable at pH 2–7, and has a half-life of up to 2 months. The development of effective methods for dimethoate degradation is therefore important. Adsorption, ultrafiltration, coagulation, and other conventional

biological and physical methods are generally used for the removal of organophosphorus pesticide pollutants from wastewater. However, these methods are expensive and produce secondary pollution [1–5]. Advanced oxidation processes have been proposed as new techniques for water treatment. Photocatalytic oxidation is efficient, environmentally friendly, and does not cause secondary pollution, and is considered to be the most promising method for dimethoate degradation.

TiO<sub>2</sub> is an important semiconductor photocatalytic material and is widely used in wastewater and air treatment. TiO<sub>2</sub> has a band gap of 3.2 eV therefore UV excitation is needed. Low solar energy use limits its practical applications. Many factors, particularly the quantum efficiency, affect the photocatalytic activity of a semiconductor material. In photocatalytic reactions, photogenerated electrons and holes act as donors and acceptors. The photocatalytic efficiency can be improved by using an electron- or hole-trapping agent to inhibit recombination of

\* Corresponding author.

\*\* Corresponding author.

\*\*\* Corresponding author.

E-mail address: [wangbaodong@nicenergy.com](mailto:wangbaodong@nicenergy.com) (B. Wang).

photogenerated electrons and holes. However, factors such as poor dispersion, recycling difficulties, and low quantum efficiencies limit applications [6–17]. In recent years, nano-TiO<sub>2</sub> loaded on molecular sieves such as 4A, ZSM-11, KIT-6, MCM-41, MCM-48, and SBA-15 have been investigated [18–28]. The TiO<sub>2</sub> loading can be varied ranging from 3 to 80 wt%. The pore structures of molecular sieves not only increase the surface areas of TiO<sub>2</sub> catalytic materials but also limit the size of the TiO<sub>2</sub> nanoparticles. This means that TiO<sub>2</sub> has a significant quantum size effect, and this increases the catalytic efficiency. SBA-15 is an ideal support material because of its large pore size, highly ordered hexagonal structure, high surface area, excellent hydrothermal stability, controllable and easily modified pore size. Its template, P123, is biodegradable. And because of its shape and framework delocalization capacity, its ability to attract electrons is better than those of other siliceous porous materials. TiO<sub>2</sub> particle linkage and dispersion inside the pores of mesoporous SBA-15 materials provide a suitable mean pore size for inducing controlled oxide particle growth and uniformity of size; the particles are stabilized, which prevents agglomeration. This approach therefore generates a large number of active sites for the adsorption/desorption of reactants or products. TiO<sub>2</sub>/SBA-15 has been used for photocatalytic decomposition of phenol, acid red 1, isoproturon, methylene blue, rhodamine B, dimethoate, alachlor, pyrimethanil, and other organic pollutants [25–34].

In most reported studies, TiO<sub>2</sub>/SBA-15 has been prepared using sol-gel and impregnation methods [29–33]. These methods tend to cause TiO<sub>2</sub> particle agglomeration. Most of them involve the use of titanium alkoxides, which are expensive, as the titanium source, an organic solvent as the medium, and multi-step hydrolysis, which is difficult to control. Rapid hydrolysis of an organic titanium source gives particles that are difficult to disperse uniformly and are therefore unsuitable for industrial production. The development of improved methods that use inexpensive materials as the titanium source for the preparation of TiO<sub>2</sub>/SBA-15 with enhanced photocatalytic activities under simulated solar light is therefore important. Ilmenite is cheap, non-toxic and widely distributed in the world which is considered the most suitable raw material for industrial production of titanium dioxide. However, no research focusing on the preparation of TiO<sub>2</sub> supported on SBA-15 molecular sieves from ilmenite and the use of such materials in the photocatalytic degradation of dimethoate has been reported.

In our previous work, high-purity nano-TiO<sub>2</sub> was prepared from Panzhihua ilmenite by liquid-phase decomposition with sulfuric acid [35]. In this study, a TiOSO<sub>4</sub> solution was obtained from ilmenite (Panzhihua, Sichuan Province, China). SBA-15 samples loaded with various amounts of TiO<sub>2</sub> were prepared using post-synthesis hydrolysis. Their photocatalytic properties and performance stability in dimethoate degradation under simulated solar light were investigated. The intermediate products and photocatalytic kinetics were also examined. The mechanism of the photocatalytic degradation of dimethoate was investigated. The technique used in this study expands the photocatalytic activity of TiO<sub>2</sub> in the visible region, and the use of ilmenite as a raw material lowers the production cost of the catalyst, facilitating industrialization.

## 2. Experimental

### 2.1. Material synthesis

#### 2.1.1. Preparation of SBA-15 mesoporous molecular sieves

SBA-15 samples were prepared hydrothermally under acidic conditions using a triblock copolymer, i.e., EO<sub>20</sub>PO<sub>70</sub>EO<sub>20</sub> (Pluronic P123, C18H36O5X2, Aldrich, China), as a template and Na<sub>2</sub>SiO<sub>3</sub>·9H<sub>2</sub>O (SINOPHARM GROUP CO.LTD., China), which is non-toxic, as the silicon source. Pluronic P123 (1 g) was dissolved in a mixture of deionized water (20 g) and 1.2 M HCl solution (50 mL, SINOPHARM GROUP CO.LTD., China) at 45 °C. The mixture was stirred for 3 h. Na<sub>2</sub>SiO<sub>3</sub>·9H<sub>2</sub>O

(5.0 g) was added and the resulting solution was stirred continuously for 10 h at 45 °C. The mixture was transferred to a Teflon-lined autoclave, kept in an oven at 110 °C for 2 d, and then aged at room temperature for 21 h. The white precipitate obtained by filtration was washed several times with deionized water and ethanol, and dried at 80 °C for 8 h. The dried product was calcined at 550 °C for 6 h.

#### 2.1.2. Preparation of TiO<sub>2</sub>/SBA-15 and pure TiO<sub>2</sub>

The mineral content of the ilmenite ore included 86.79 wt% ilmenite, 5.32 wt% rutile, 4.40 wt% quartz, 3.11 wt% hematite and 0.38 wt% microcline. The chemical composition analysis of ilmenite is 4.78 wt% SiO<sub>2</sub>, 43.6 wt% TiO<sub>2</sub>, 2.10 wt% Al<sub>2</sub>O<sub>3</sub>, 3.11 wt% Fe<sub>2</sub>O<sub>3</sub>, 34.45 wt% FeO and others [35]. Liquid-phase Panzhihua ilmenite decomposition was performed using sulfuric acid (13.5 mol/L) at 160 °C for 120 min. The titanium solution with certain iron ions may reduce the quality of as-prepared TiO<sub>2</sub>. Thus the Fe<sup>3+</sup> should be reduced to Fe<sup>2+</sup> using iron powder as a reducing agent. The ferrous sulfate could be separated after cooling and crystallization according to our previous research [35]. The resulting pure TiOSO<sub>4</sub> solution contained 121 g/L Ti<sup>4+</sup>. TiO<sub>2</sub>/SBA-15 samples were prepared by post-synthesis hydrolysis. Calcined SBA-15 (0.3 g) was dispersed in ethanol (20 mL) with continuous stirring. The required amount of deionized water was added to the suspension, and a solution with a TiOSO<sub>4</sub> solution (0.2 mL, 0.4 mL, 0.7 mL, 0.9 mL and 1.1 mL): deionized water volume ratio of 1:9 was added slowly. The suspension was stirred for 3 h at 90 °C and then aged at room temperature for 28 h. The products were obtained by filtration, washed consecutively with deionized water and ethanol, and then dried at 80 °C for 1 h. The synthesized materials were calcined in a tubular furnace at 550 °C for 6 h. Pure TiO<sub>2</sub> particles were also prepared using the same procedure and their photocatalytic properties were compared with those of SBA-15.

### 2.2. Photocatalytic degradation experiments

Photocatalytic degradation of dimethoate (99.5%, Institute for Reference Materials, China; the chemical structure of dimethoate is shown in Fig. 1) under simulated solar light, provided using a 500-W xenon lamp (Beijing Dian Guang, China, light intensity 1000 W/m<sup>2</sup>), was used to evaluate the photocatalytic properties of the synthesized materials as follows. Mineralization was followed by measuring the total organic carbon (TOC) by direct injection of filtered samples into a Shimadzu-5050A TOC analyser provided with an NDIR detector and calibrated with standard solutions of potassium phthalate. H<sub>2</sub>O<sub>2</sub> (0.03 mL, 30%) was added to dimethoate solution (30 ppm, 900 mL) as an oxidant and the pH was adjusted to 12 using NaOH (0.1 mol/L). The experiments were performed using TiO<sub>2</sub>/SBA-15 samples (1.5 g) under ultrasonic agitation for 10 min. Before irradiation, the suspension was stirred in the photocatalytic reactor vessel in the dark for 30 min to achieve adsorption-desorption equilibrium. Magnetic stirring was maintained throughout. Suspension samples (5 mL) were collected at certain time intervals and centrifuged to remove the catalyst. Degradation experiments in the presence of pure TiO<sub>2</sub> and in the absence

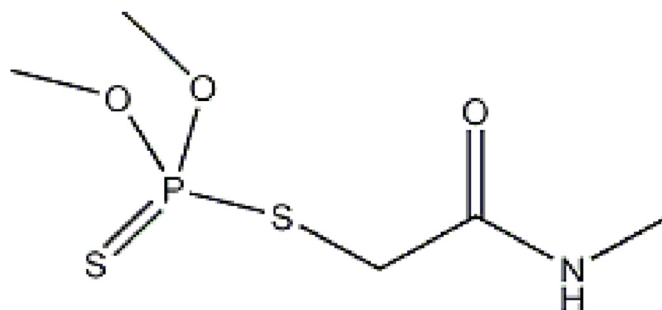


Fig. 1. Dimethoate structure.

of any catalyst or irradiation were also conducted for comparison. The amount of dimethoate degraded was indirectly determined using the concentration of phosphate because the generation of phosphate stoichiometrically represent the degradation of dimethoate, with 1 mol of phosphate released for each mole of dimethoate. The concentration of phosphate was determined using the phosphomolybdate blue method [12]. The efficiency was defined as:

$$x\% = \frac{C_0 - C_t}{C_0} \times 100\% \quad (1)$$

where  $C_0$  is the original concentration of dimethoate and  $C_t$  is the concentration of dimethoate remaining at time  $t$ .

The stability of the  $\text{TiO}_2/\text{SBA-15}$  catalyst was investigated by performing recycling experiments. The used catalysts were collected by centrifugation after dimethoate photodegradation, washed with deionized water and ethanol, and dried at 80 °C for 2 h. The used catalyst was used to degrade a fresh dimethoate solution (30 mg/mL) under the same conditions. The process was repeated three times. The  $\text{TiO}_2/\text{SBA-15}$  catalyst collected after the third cycle was calcined at 550 °C for 6 h and reused.

### 2.3. Characterization

X-ray diffraction (XRD) was performed using a D/Max-RA diffractometer (Rigaku, Japan), using  $\text{Cu K}\alpha$  radiation and a step size of 0.02° in the scanning range 10–80° at a scanning rate of 3°/min, or in the range 0.5–5° at a rate of 0.3°/min. Fourier-transform infrared (FT-IR) spectroscopy was performed using the KBr method (TENSOR-27, Bruker, Germany). Raman spectra were recorded using a micro-Raman spectrometer (Renishaw inVia, UK) with a 514 nm  $\text{Ar}^+$  laser as an excitation source. High-resolution transmission electron microscopy (HRTEM) was performed using a Hitachi JEM-3010 instrument (Japan). Diffusion-reflectance ultraviolet-visible (UV-vis) spectra were recorded using a UV-3600 spectrometer (Shimadzu) with barium sulfate as the base material; the scanning range was 200–800 nm. Nitrogen adsorption-desorption isotherms were recorded, using an AUTOSORB-1MP automatic physical adsorption instrument, at 77 K after degassing the samples at 373 K. Gas chromatography-mass spectrometry (GC/MS) was performed using a Thermo Trace 1300-ISQ GC/MS system (Thermo, USA) equipped with a TR-5MS column. The phosphate ions were analyzed spectrophotometrically with a WTW spectrophotometer. The  $\text{TiO}_2$  loadings of the  $\text{TiO}_2/\text{SBA-15}$  matrices were determined by inductively coupled plasma atomic emission spectroscopy (ICP-AES), Perkin Elmer Optima 3300DV.

## 3. Results and discussion

### 3.1. Characterization of the SBA-15 support

The prepared SBA-15 mesoporous molecular sieves can produce a three-dimensional pore structure through hydrothermal treatment at more than 100 °C. That is, main pore channels are produced and disordered microporous and mesoporous tunnels are obtained. The pore structure and structural characteristics of the SBA-15 molecular sieve are shown in Figs. 2–4.

Fig. 2 shows low-angle X-ray diffraction results of the SBA-15. The XRD pattern of SBA-15 showed four peaks that could be indexed as (1 0 0), (1 1 0), (2 0 0), and (2 1 0) reflections corresponding to p6mm hexagonal symmetry.

Figs. 3 and 4 are nitrogen adsorption and desorption curves and pore size distributions of the SBA-15 molecular sieve, respectively. Fig. 2 shows that this molecular sieve belongs to a type IV curve typical of the IUPAC classification, suggesting a mesoporous structure. The nitrogen adsorption and desorption curves showed clear mutations between the relative pressure  $p/p_0 = 0.4$ –0.8, caused by capillary condensation, which belongs to H1 type hysteresis loop. The pore size

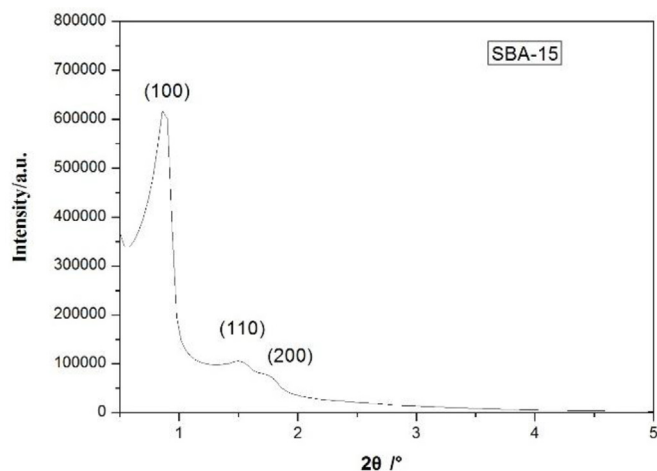


Fig. 2. Small-angle XRD pattern of prepared SBA-15 molecular sieves.

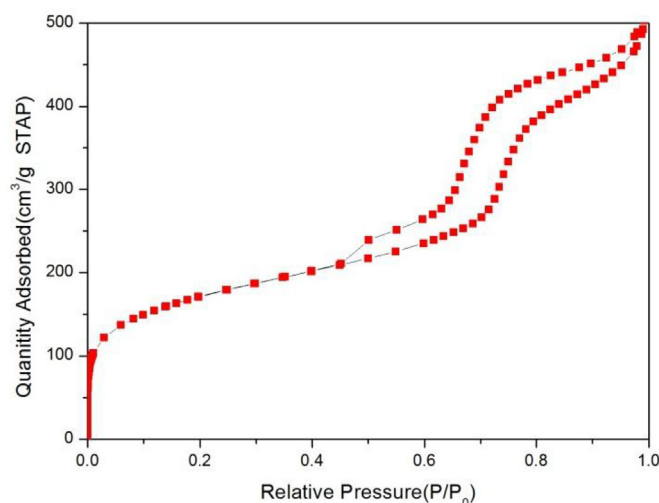


Fig. 3. BET specific surface area of SBA-15 molecular sieves.

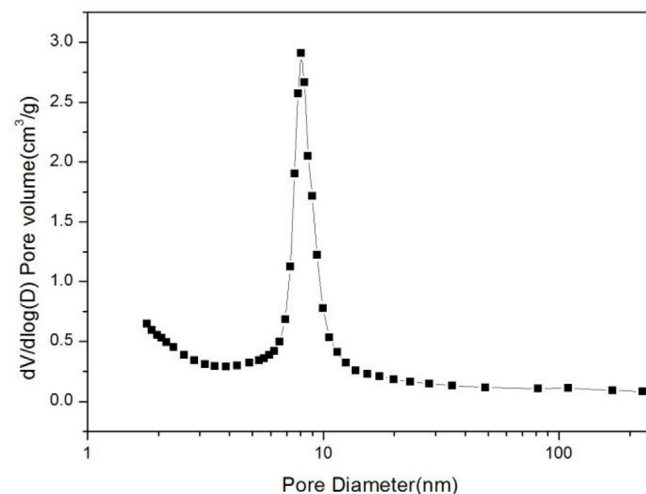


Fig. 4. Pore size distribution of fly ash-derived SBA-15 molecular sieve.

distribution in Fig. 3 indicates that the material had a highly ordered mesoporous structure, uniform pore size distribution, and regular pores. The BET surface area of the prepared fly ash-derived SBA-15 molecular sieve was 793.59  $\text{m}^2/\text{g}$ , the pore volume was 0.748  $\text{cm}^3/\text{g}$ , and the average pore diameter was 6.11 nm

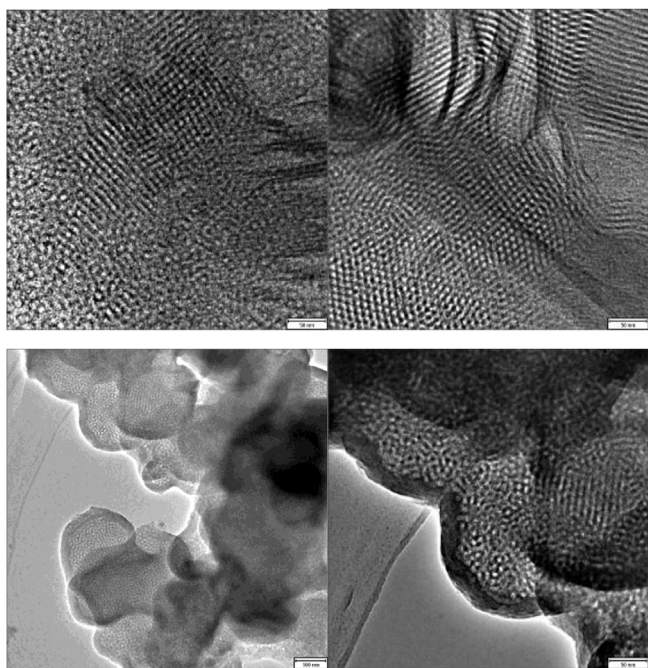


Fig. 5. TEM of fly ash-derived SBA-15 molecular sieves.

Fig. 5 shows transmission electron microscope images of the SBA-15 molecular sieve sample. The figure shows that the pores of the SBA-15 molecular sieve were regular and hexagonal, and the skeleton was orderly arranged, the pore diameter was approximately 5 nm, and the thickness of the pore wall was approximately 3 nm.

### 3.2. Photocatalytic properties of $\text{TiO}_2/\text{SBA-15}$

Fig. 6 shows the photocatalytic decomposition of dimethoate solution using  $\text{TiO}_2/\text{SBA-15}$  catalysts with various  $\text{TiO}_2$  loadings. The figure shows that the photocatalytic activity increased with increasing  $\text{TiO}_2$  loading from 8% to 26%. However, the photocatalytic activity decreased with increasing  $\text{TiO}_2$  loading from 26% to 42%. This may be because the catalyst with a 26%  $\text{TiO}_2$  loading has the most suitable specific surface area, and this is conducive to reactant adsorption on the

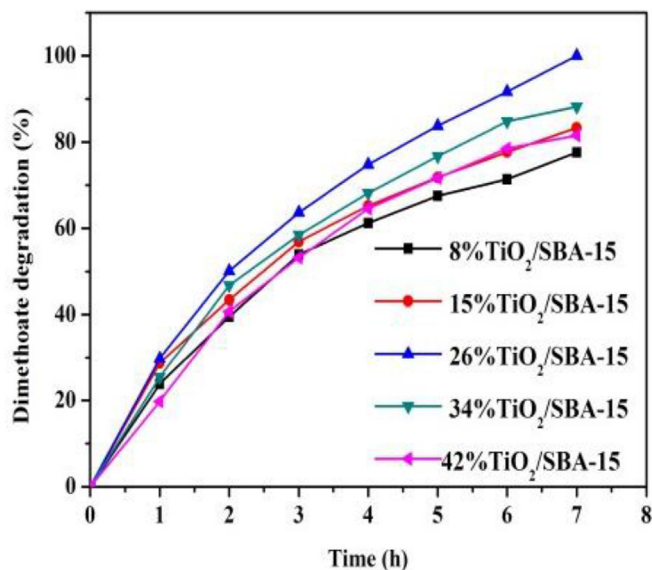


Fig. 6. Photocatalytic performances of  $\text{TiO}_2/\text{SBA-15}$  samples with various  $\text{TiO}_2$  loadings.

catalyst, and the  $\text{TiO}_2$  particles can be well dispersed on the molecular sieve surfaces, which is conducive to electron–hole separation. A larger number of surface active sites increases the photocatalytic activity. When the  $\text{TiO}_2$  loading is lower than 26%, although the catalyst has a large specific surface area,  $\text{TiO}_2$  is not well dispersed on the molecular sieves. The amount of dispersed  $\text{TiO}_2$  is a key factor in the photocatalytic activity, and poor dispersion decreases the catalytic activity. When the  $\text{TiO}_2$  loading is higher than 26%, some of the  $\text{TiO}_2$  particles agglomerate on the SBA-15, and the poor dispersion decreases the photocatalytic efficiency. The photocatalytic properties of the  $\text{TiO}_2/\text{SBA-15}$  catalyst depend on the crystallinity, specific surface area, and particle size and dispersion. The decline in the degradation rate at high loadings can be explained as follows. (i) Blocking of the mesopores of SBA-15 by excess  $\text{TiO}_2$  results in a decrease in the adsorption capacity. (ii) The electrons produced from the excited  $\text{TiO}_2$  particles, which are not close to the support surface, are not delocalized, resulting in faster electron and hole recombination, causing lower degradation rates [28,29]. The enhancement of the catalytic reactivity is also can be explained by a condensation of reactants. A complete degradation of an organic molecule by photocatalysis normally leads to the conversion of all its carbon atoms to gaseous  $\text{CO}_2$ , and the heteroatoms into inorganic anions that remain in the solution.

These results show that optimization of the  $\text{TiO}_2$  loading is necessary to achieve effective synergism between the active sites of  $\text{TiO}_2$  and the adsorption properties of the support. The role of the support during photocatalytic degradation was clarified by performing comparative studies using bare pure  $\text{TiO}_2$ . Fig. 7 shows that the catalytic performance of  $\text{TiO}_2/\text{SBA-15}$  is much better than that of pure  $\text{TiO}_2$ . This may be because of the synergistic effect resulting from the adsorption of dimethoate on the mesoporous material. This can facilitate the degradation without affecting the photocatalytic properties of  $\text{TiO}_2$ . The delocalization of electrons on the SBA-15 framework and adsorption properties of the support enhance the degradation rate. The dispersion of  $\text{TiO}_2$  on the mesoporous material hinders particle–particle aggregation and light scattering by  $\text{TiO}_2$ . Good dispersion leads to the presence of more active sites near the adsorbed dimethoate molecules, resulting in faster degradation rates. In addition, the  $\text{TiOSO}_4$  solution was obtained from ilmenite, a small amount of iron ion was certainly present in the  $\text{TiOSO}_4$  solution, although after the iron removal process [35]. The  $\text{Fe}^{3+}$  is highly effective for  $\text{H}_2\text{O}_2$  dissociation under light irradiation. 26%  $\text{TiO}_2/\text{SBA-15}$  had the highest catalytic activity in dimethoate degradation and was chosen for further studies. When dimethoate degradation was performed under irradiation but without a catalyst, the degradation rate was 3.7%; this is probably because of direct decomposition of the organic compound by absorbed light energy rather than

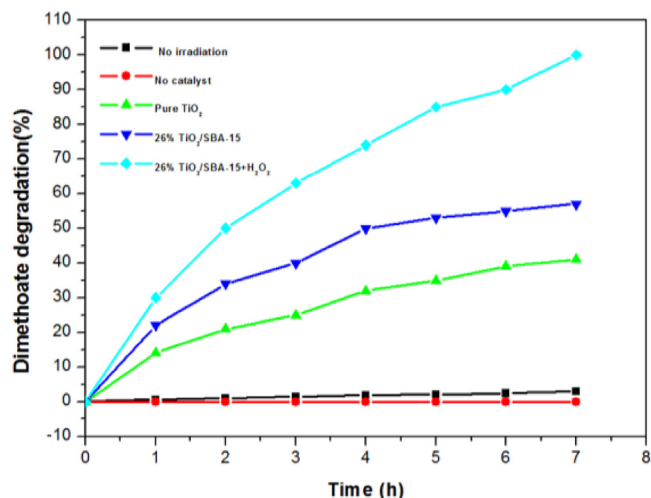


Fig. 7. Photocatalytic degradation of dimethoate under various conditions.

by reaction with an oxidant such as  $\text{H}_2\text{O}_2$  or  $\text{O}_2$ . The addition of an oxidant to a semiconductor suspension enhances the photodegradation rates for various organic pollutants [26–30]. This is because hydrogen peroxide can act as an electron acceptor and can therefore promote charge separation. It can also produce  $\text{OH}^\bullet$  radicals, according to equations (2) and (3). The ability of  $\text{H}_2\text{O}_2$  to enhance the photodegradation of dimethoate is not only due to the entrapment of the photogenerated electrons, but also due to their own ability to absorb light and act as sensitizers through the production of hydroxyl and sulfate radicals. No dimethoate degradation occurred in the absence of both a catalyst and irradiation. The photocatalytic activity of 26%  $\text{TiO}_2/\text{SBA-15}$  without  $\text{H}_2\text{O}_2$  was significantly lower than that of the 26%  $\text{TiO}_2/\text{SBA-15}$  in the presence of  $\text{H}_2\text{O}_2$  as the oxidant. Without oxidant, the photocatalytic efficiency is only about 50%, in the presence of  $\text{H}_2\text{O}_2$ , photocatalytic degradation of dimethoate can reach to 100%.



### 3.3. Characterization of $\text{TiO}_2/\text{SBA-15}$

#### 3.3.1. XRD analysis

The XRD patterns of pure SBA-15, pure  $\text{TiO}_2$ , and SBA-15 samples with various  $\text{TiO}_2$  loadings are shown in Fig. 8. The new diffraction peaks in the  $\text{TiO}_2/\text{SBA-15}$  samples, at  $25.41^\circ$ ,  $37.89^\circ$ ,  $48.09^\circ$ ,  $53.97^\circ$ ,  $55.12^\circ$ , and  $62.73^\circ$ , are assigned to the (101), (004), (200), (105), (211), and (204) anatase planes, respectively. The peak intensities increased with increasing titanium content. The three peaks indexed to the (100), (110), and (200) planes are characteristic of a mesoporous structure with two-dimensional (2D) hexagonal symmetry. The (100) plane peak was present regardless of the  $\text{TiO}_2$  loading. This indicates that the silica framework was stable and retained after  $\text{TiO}_2$  incorporation. The decrease in the intensity of the (100) plane with increasing  $\text{TiO}_2$  loading may be caused by the presence of a small amount of  $\text{TiO}_2$  in the pore channels, which would make the molecular sieve structure slightly less ordered. The Scherrer formula is,

$$D = 0.89\lambda/\beta\cos\theta, \quad (4)$$

where  $D$  is the average crystal size,  $\lambda$  is X-ray wavelength ( $1.5406 \text{ \AA}$ ),  $\beta$

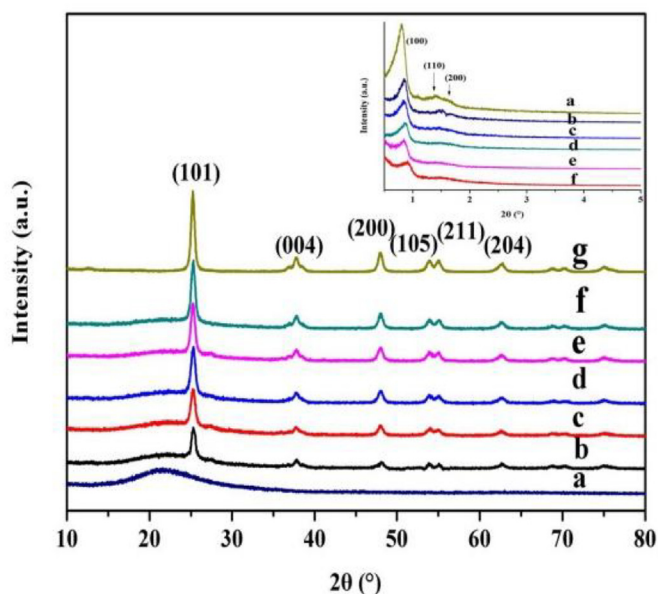


Fig. 8. XRD patterns of (a) SBA-15; SBA-15 loaded with (b) 8, (c) 15, (d) 26, (e) 34, and (f) 42 wt%  $\text{TiO}_2$ ; and (g)  $\text{TiO}_2$  (inset shows small-angle XRD patterns).

Table 1

Crystallite size of the metal oxide in  $\text{TiO}_2/\text{SBA-15}$  and cell parameters of SBA-15.

Photocatalyst	Crystallite size (nm)	$a_0$ (nm)
8% $\text{TiO}_2/\text{SBA-15}$	2.32	12.75
15% $\text{TiO}_2/\text{SBA-15}$	2.79	12.63
26% $\text{TiO}_2/\text{SBA-15}$	3.02	12.55
34% $\text{TiO}_2/\text{SBA-15}$	3.44	12.53
42% $\text{TiO}_2/\text{SBA-15}$	4.56	12.41

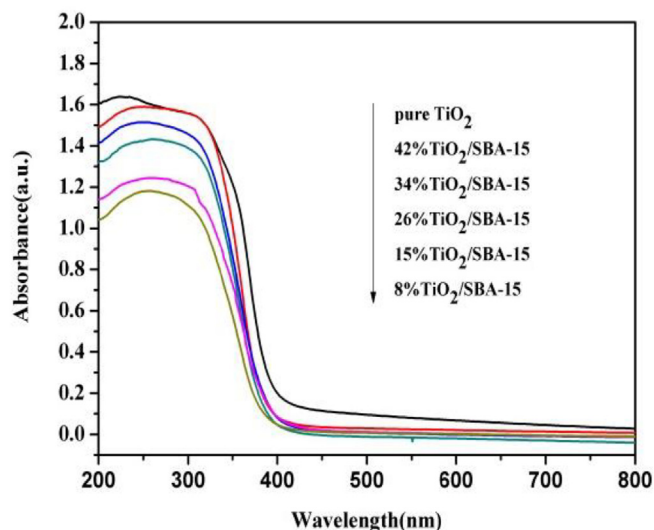


Fig. 9. UV-vis diffuse reflectance spectra of pure  $\text{TiO}_2$  and  $\text{TiO}_2/\text{SBA-15}$  samples with different  $\text{TiO}_2$  loadings.

is the full width at half maximum of the most intense diffraction peak, and  $\theta$  is the diffraction angle at the peak maximum. The crystallite size of  $\text{TiO}_2$  in  $\text{TiO}_2/\text{SBA-15}$  was calculated according to Equation (4); the results are shown in Table 1. As the doped  $\text{TiO}_2$  content increased for  $\text{TiO}_2/\text{SBA-15}$  samples, the catalyst crystallite size increased.

#### 3.3.2. UV-vis spectra

The diffuse-reflectance UV-vis spectra of pure  $\text{TiO}_2$  and  $\text{TiO}_2/\text{SBA-15}$  samples are shown in Fig. 9. The figure clearly shows that the absorption band edges of all the  $\text{TiO}_2/\text{SBA-15}$  samples were significantly blue-shifted compared with that of pure  $\text{TiO}_2$ . The absorption band edges also blue-shifted with decreasing of  $\text{TiO}_2$  content, because of the quantum size effect. These results show that SBA-15 effectively suppresses the growth of  $\text{TiO}_2$  nanoparticles. This improves the photocatalytic properties.

#### 3.3.3. Porosity characterization

Fig. 10 shows HRTEM images of SBA-15 and  $\text{TiO}_2/\text{SBA-15}$  samples. The figure clearly shows a highly ordered 2D hexagonal structure with pores of diameter 8.50 nm and wall thickness 3 nm. The SBA-15 hexagonal structure was maintained after  $\text{TiO}_2$  loading; the pore diameter was 8.08 nm and the pore wall thickness was 3.8 nm. The slight decrease in the pore diameter was probably caused by some of the  $\text{TiO}_2$  grains blocking the mesopores channels. These pores result in a high specific surface area, which facilitates contact between the reactants and the catalyst, and improves the photocatalytic activity.

The nitrogen adsorption isotherms and pore size distributions of SBA-15 and  $\text{TiO}_2/\text{SBA-15}$  are shown in Fig. 11. The SBA-15 sample had a type IV isotherm with an H1 hysteresis loop; this is typical of mesoporous materials with ordered and uniform pore structures. The basic structure was not changed by  $\text{TiO}_2$  loading. However, the data in Table 2 show that the surface area and pore size decreased slightly after

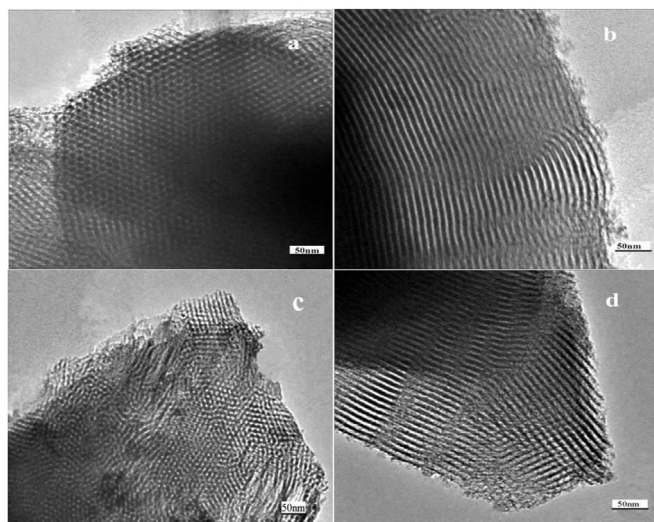


Fig. 10. HRTEM images of (a and b) SBA-15 and (c and d) 26% TiO<sub>2</sub>/SBA-15.

TiO<sub>2</sub> loading. This may be caused by TiO<sub>2</sub> nanoparticle incorporation into the SBA-15 channels, and is consistent with the XRD and HRTEM results.

The quantities of TiO<sub>2</sub> present in the synthesized x% TiO<sub>2</sub>/SBA-15 samples were determined using ICP-AES. The results are listed in Table 2. The data in the table show that the TiO<sub>2</sub> contents of the hybrid materials were 8.2–41.5 wt%. Catalyst samples with the target TiO<sub>2</sub> contents were obtained using this post-synthesis technique.

### 3.3.4. FT-IR spectra

The FT-IR spectra of pure SBA-15, pure TiO<sub>2</sub>, and TiO<sub>2</sub>/SBA-15 are shown in Fig. 12. The peaks at 3442 and 1630 cm<sup>-1</sup> are attributed to O–H stretching and bending vibrations, respectively, from water chemically adsorbed on Lewis acid sites. The peaks at 800 and 1088 cm<sup>-1</sup> in the SBA-15 spectrum are assigned to Si–O–Si symmetric and asymmetric stretching vibrations, respectively. The peak at 464 cm<sup>-1</sup> is attributed to the Si–O–Si bending vibration. The broad peak at 400–600 cm<sup>-1</sup> in the pure TiO<sub>2</sub> spectrum is typical of Ti–O–Ti. Fig. 12(b) shows that for the TiO<sub>2</sub>/SBA-15 sample, the Si–O–Si and Ti–O–Ti peaks overlap at 464 cm<sup>-1</sup>. Shifts in the peaks at 965 and

**Table 2**  
Chemical, specific surface areas ( $A_{\text{BET}}$ ), pore volumes ( $V_{\text{B,H}}$ ), and pore sizes ( $D_{\text{B,H}}$ ) of SBA-15 and TiO<sub>2</sub>/SBA-15.

Sample	BET Specific surface area/ (m <sup>2</sup> ·g <sup>-1</sup> )	Average pore volume/ (cm <sup>3</sup> ·g <sup>-1</sup> )	Average pore size/nm	TiO <sub>2</sub> (wt.%)
SBA-15	861	0.9891	8.50	–
8%TiO <sub>2</sub> /SBA-15	775	0.9803	8.42	8.2
15%TiO <sub>2</sub> /SBA-15	721	0.9798	8.33	14.6
26%TiO <sub>2</sub> /SBA-15	686	0.9769	8.08	26.2
34%TiO <sub>2</sub> /SBA-15	662	0.9721	7.99	34.4
42%TiO <sub>2</sub> /SBA-15	569	0.9635	7.56	41.5

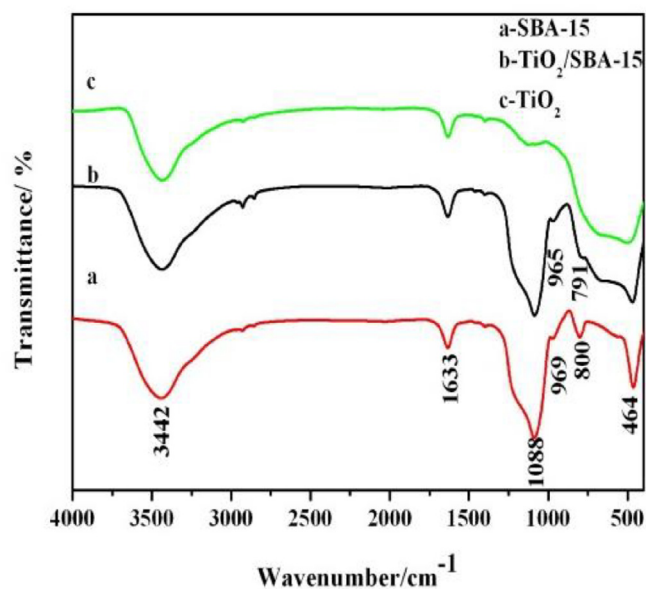


Fig. 12. FT-IR spectra of (a) SBA-15, (b) 26 wt% TiO<sub>2</sub>/SBA-15, and (c) TiO<sub>2</sub>.

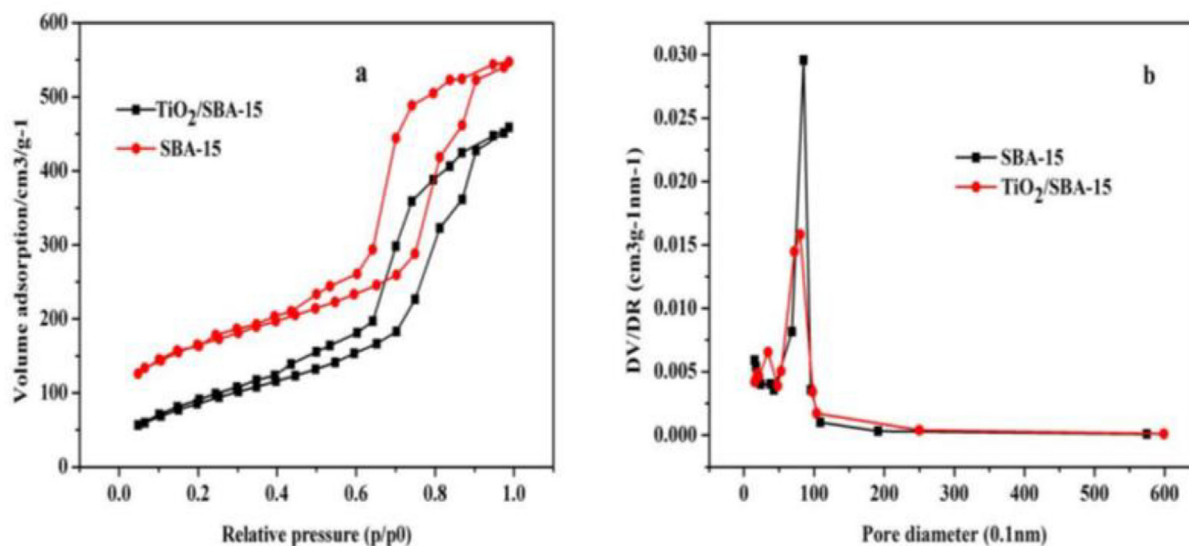


Fig. 11. Nitrogen adsorption isotherms for (a) SBA-15 and 26% TiO<sub>2</sub>/SBA-15, and (b) pore size distributions for SBA-15 and 26% TiO<sub>2</sub>/SBA-15.

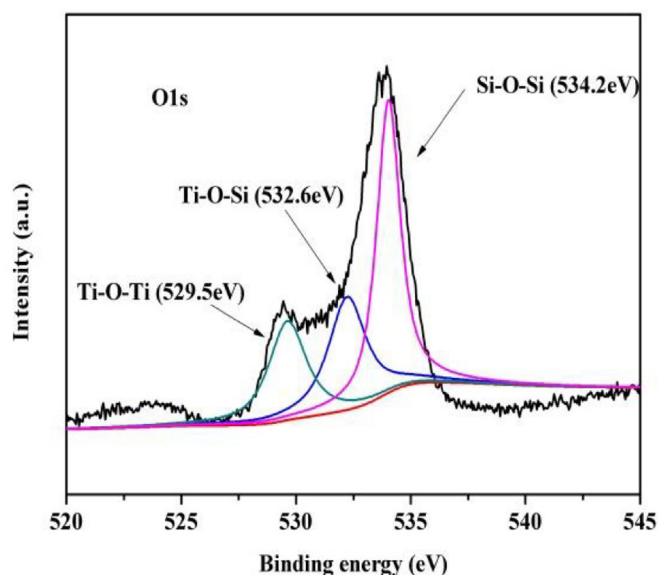


Fig. 13. XPS spectra of 26% TiO<sub>2</sub>/SBA-15.

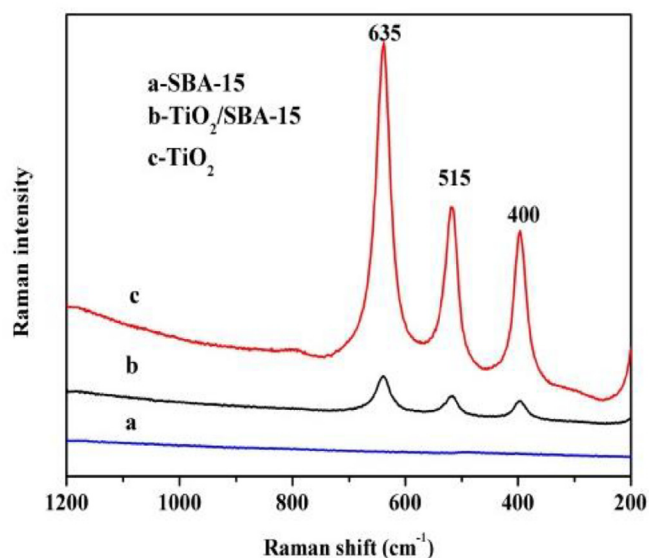


Fig. 14. Raman spectra of (a) SBA-15, (b) 26% TiO<sub>2</sub>/SBA-15, and (c) TiO<sub>2</sub>.

791 cm<sup>-1</sup> were observed. The shift in the 965 cm<sup>-1</sup> peak is attributed to combination of the stretching vibrations of the Si–O– species in Si–OH groups and in Ti<sup>4+</sup>–Si–O species involving tetrahedrally coordinated Ti<sup>4+</sup> ions [30–32]. The other peak shift is attributed to combination of the stretching vibrations of Si–O–Si and Ti–O–Ti. These features indicate the presence of Ti–O–Si bonding between SBA-15 and TiO<sub>2</sub>.

### 3.3.5. XPS spectra

The XPS spectra of the 26% TiO<sub>2</sub>/SBA-15 sample is shown in Fig. 13. The O 1s XP spectrum shows three peaks, at 534.2, 532.6, and 529.5 eV, which are attributed to oxygen in Si–O–Si, Ti–O–Si, and Ti–O–Ti, respectively. The peak at 532.6 eV indicates Ti–O–Si formation between SBA-15 and TiO<sub>2</sub> and is consistent with the FT-IR results. It is important to note that Ti–O–Si species can form TiO<sub>2</sub> surface defects, and photogenerated electrons can easily migrate to the surface, further reducing the probability of electron–hole combination. The Ti–O–Si species also enhance the TiO<sub>2</sub> surface acidity, resulting in formation of a larger number of surface adsorption sites; this improves

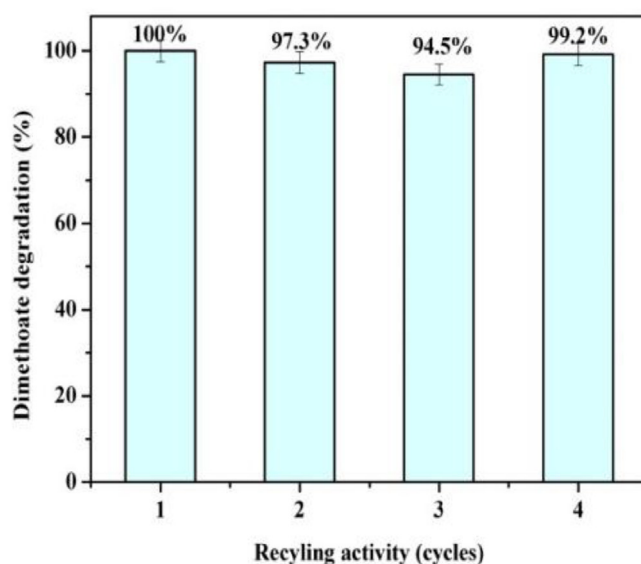


Fig. 15. Dimethoate photocatalytic degradation ability of 26% TiO<sub>2</sub>/SBA-15 as function of cycle number.

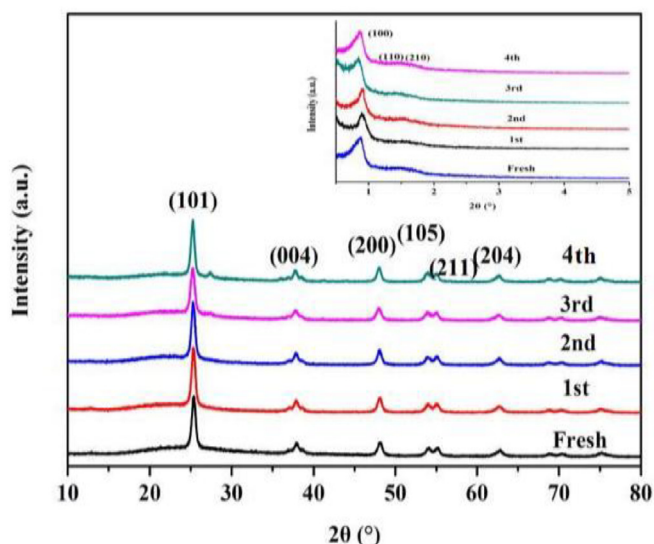


Fig. 16. XRD patterns of 26% TiO<sub>2</sub>/SBA-15 after different cycles (catalyst in fourth cycle was calcined before use; inset shows small-angle XRD patterns).

the photocatalytic activities of the TiO<sub>2</sub>/SBA-15 catalysts [27–29].

### 3.3.6. Raman spectra

The Raman spectra of SBA-15, 26% TiO<sub>2</sub>/SBA-15, and TiO<sub>2</sub> samples are shown in Fig. 14. Fig. 14(a) shows that the SBA-15 spectrum shows no clear peaks. Fig. 14(b) shows that TiO<sub>2</sub> loading significantly changed the SBA-15 spectrum. The Raman peaks at 400, 515, and 635 cm<sup>-1</sup> correspond to the B<sub>1g</sub>(1), B<sub>1g</sub>(2), and E<sub>g</sub>(3) modes, respectively, of anatase. The TiO<sub>2</sub>/SBA-15 peak intensities are clearly weaker than those for pure TiO<sub>2</sub>; this is consistent with the XRD patterns.

### 3.4. Reusability and recyclability of TiO<sub>2</sub>/SBA-15 catalyst

Catalyst reusability is one of the most important factors in practical applications of photocatalytic degradation. Fig. 15 shows that TiO<sub>2</sub>/SBA-15 retained high catalytic activity after four consecutive runs. The degradation rate decreased by 5.5% from the first to the third cycle. This is probably because of the adsorption of intermediate products on

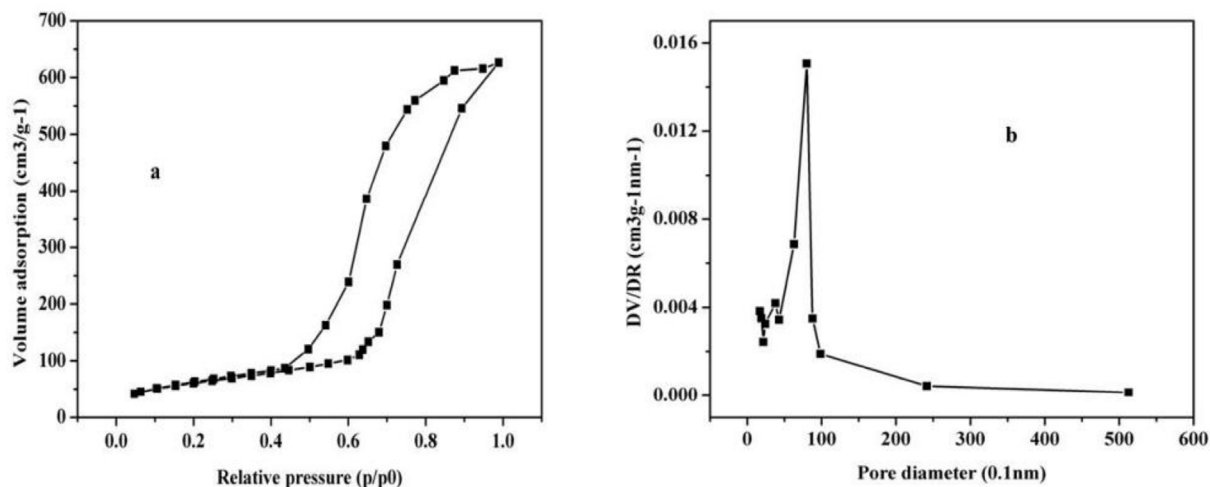


Fig. 17. Nitrogen adsorption isotherms of  $\text{TiO}_2/\text{SBA-15}$  after four cycles.

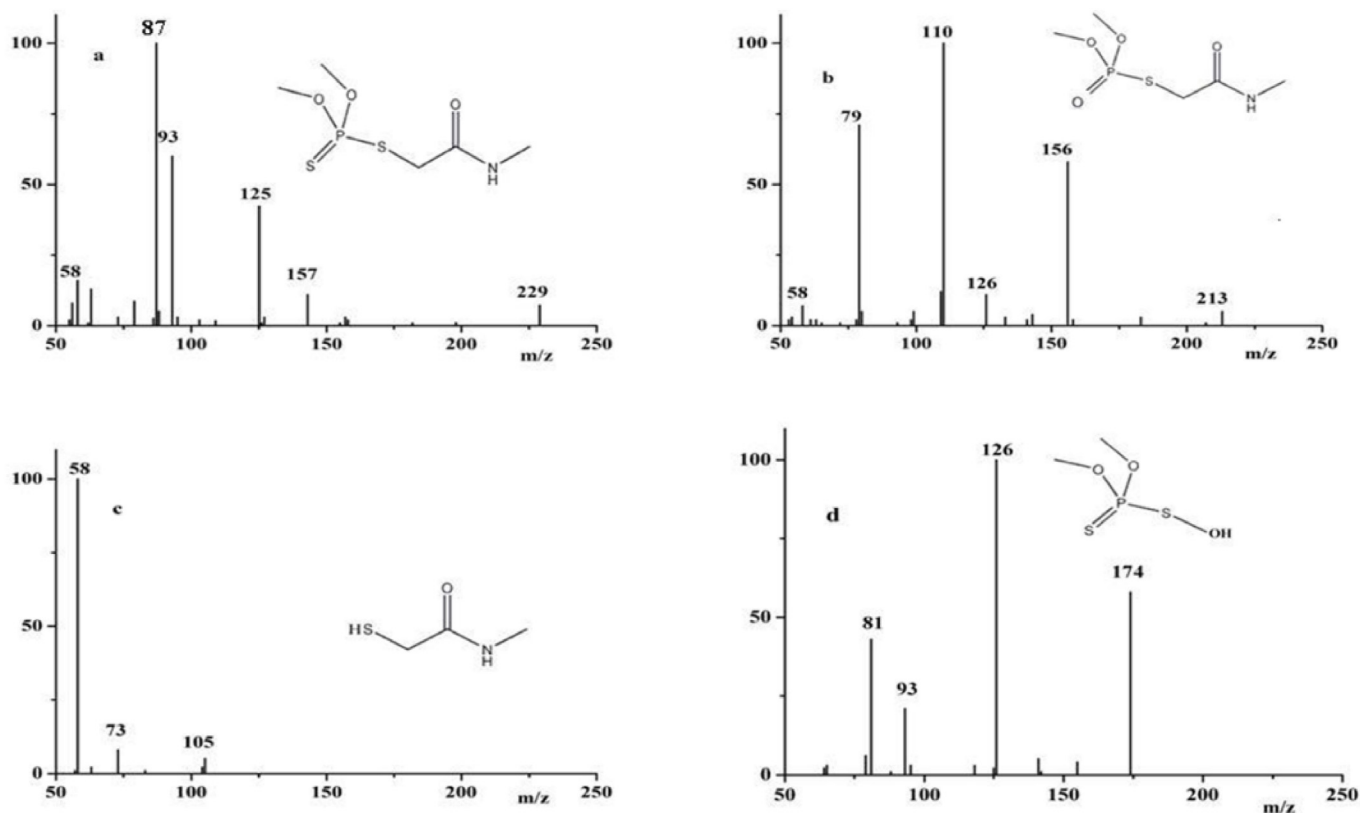


Fig. 18. Mass spectra of degradation products formed during photocatalytic degradation in presence of 26%  $\text{TiO}_2/\text{SBA-15}$  catalyst (degradation time 4 h).

the catalyst, which affects dimethoate adsorption and reduces the catalytic activity. Fig. 15 shows that the activity of the calcined reused catalyst in the fourth cycle was the same as that of the fresh catalyst. This shows that calcination is necessary to regenerate the activity of the used catalyst. Fig. 16 shows the XRD patterns of the used catalysts; the samples were intact even after the fourth cycle. The characteristic peaks of the  $\text{TiO}_2$  phase and SBA-15 mesoporous material in the used catalyst do not differ significantly from those of the fresh sample. This may be because calcination removes some of the intermediates adsorbed on the catalyst surface, therefore the catalytic performance is maintained. Fig. 17 shows the adsorption isotherms and pore size distributions of the 26%  $\text{TiO}_2/\text{SBA-15}$  catalyst after four cycles. The sample still had a

type IV isotherm with an H1 hysteresis loop, indicating that the ordered mesoporous structure was unchanged. The pore size changed slightly, from 8.08 to 7.97 nm. These results indicate that the catalyst was highly stable and its photocatalytic activity was basically maintained after reuse for several cycles.

### 3.5. Intermediate product analysis

We investigated the dimethoate decomposition pathway by analyzing the intermediate products. The organic products formed during photocatalytic oxidation were identified using GC-MS. The main intermediates detected in a solution irradiated with simulated solar light

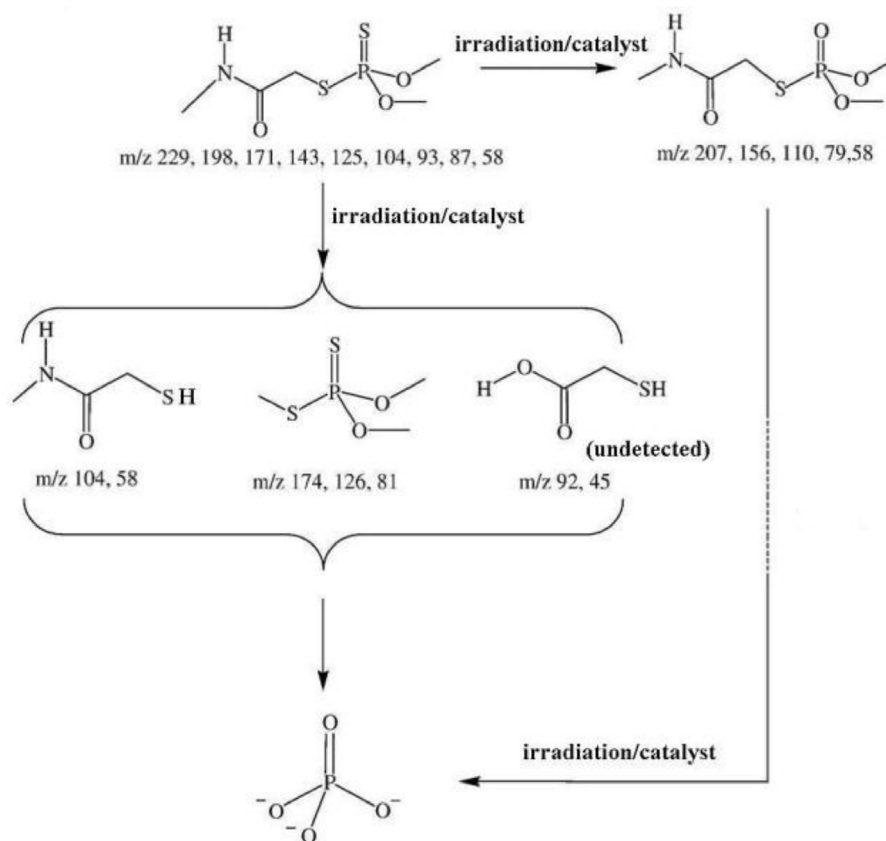


Fig. 19. Possible pathway for photocatalytic degradation of dimethoate.

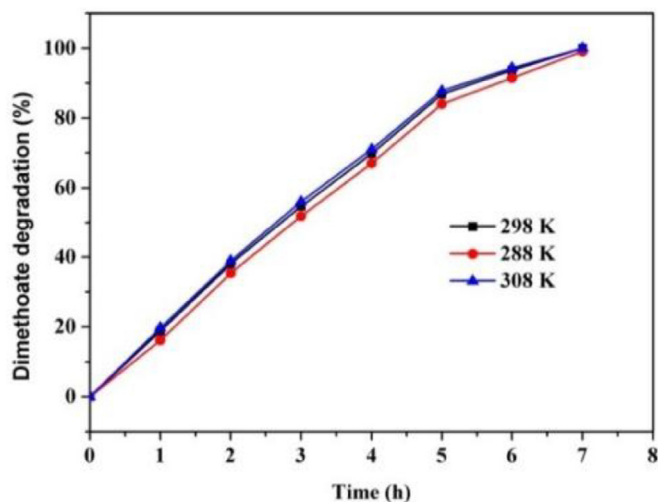


Fig. 20. Photocatalytic degradation of dimethoate at various temperatures.

Table 3  
Kinetic equation at various temperatures.

Temperature/K	Rate equation	Rate constants (mg·L <sup>-1</sup> ·h <sup>-1</sup> )	The correlation coefficient/R <sup>2</sup>
288	ln(C <sub>0</sub> /C <sub>t</sub> ) = 0.321t - 0.165	0.321	0.98973
298	ln(C <sub>0</sub> /C <sub>t</sub> ) = 0.327t - 0.145	0.327	0.99155
308	ln(C <sub>0</sub> /C <sub>t</sub> ) = 0.335t - 0.140	0.335	0.99164

for 4 h are shown in Fig. 18. Four organic byproducts, i.e., dimethoate, omethoate, *N*-methyl-2-sulfanylacetamide, and *O,O,S*-trimethyl thiophosphorothioate, were detected, and identified using the NIST library. Fig. 18(a) shows that dimethoate gave a molecular ion peak with *m/z* 229, and peaks with *m/z* 125 and 93, corresponding to [(CH<sub>3</sub>O)<sub>2</sub>P(S)]<sup>+</sup> and [(CH<sub>3</sub>O)<sub>2</sub>P]<sup>+</sup> ions, respectively. Fig. 18(b) shows that omethoate was identified based on the molecular ion peak with *m/z* 213 and a characteristic ion peak with *m/z* 156. The *m/z* 156 ion rearranges by hydrogen migration to the phosphoryl oxygen, accompanied by loss of neutral *N*-methyl isocyanate from omethoate, and the *m/z* 110 ion is formed by cleavage accompanied by migration of hydrogen. This indicates that dimethoate was partly oxidized to the more toxic omethoate. Fig. 18(c) shows that *N*-methyl-2-sulfanylacetamide was identified based on the molecular ion with *m/z* 105 and the ions at *m/z* 73 and 58, which correspond to the loss of HSCH<sub>2</sub><sup>-</sup> and HS<sup>-</sup> fragments, respectively. Fig. 18(d) shows that *O,O,S*-trimethyl thiophosphorothioate was identified based on the ion peak with *m/z* 93, which corresponds to the [(CH<sub>3</sub>O)<sub>2</sub>P]<sup>+</sup> group, a peak with *m/z* 174, which corresponds to the molecular ion [M]<sup>+</sup>, and the ions with *m/z* 126 and 81, which correspond to the loss of HOS<sup>-</sup>, CH<sub>3</sub><sup>-</sup>, and CHO<sub>3</sub><sup>-</sup> fragments. Dimethoate was finally mineralized to PO<sub>4</sub><sup>3-</sup>, SO<sub>4</sub><sup>2-</sup>, NO<sub>3</sub><sup>-</sup>, CO<sub>2</sub>, and H<sub>2</sub>O. The proposed degradation pathway (Fig. 19) is consistent with that in the literature [36,37]. The photocatalytic degradation of organic compounds such as pesticides is a complex process and involves interconnected pathways leading to the formation of various transformation products that were not investigated in this study. We propose that the photocatalytic degradation of pesticides mainly occurs via photocatalytic oxidation reactions initiated by strongly oxidizing species such as hydroxyl radicals and/or superoxide anion radicals.

No toxic materials such as omethoate, *N*-methyl-2-sulfanylacetamide, and *O,O,S*-trimethyl thiophosphorothioate were detected in the

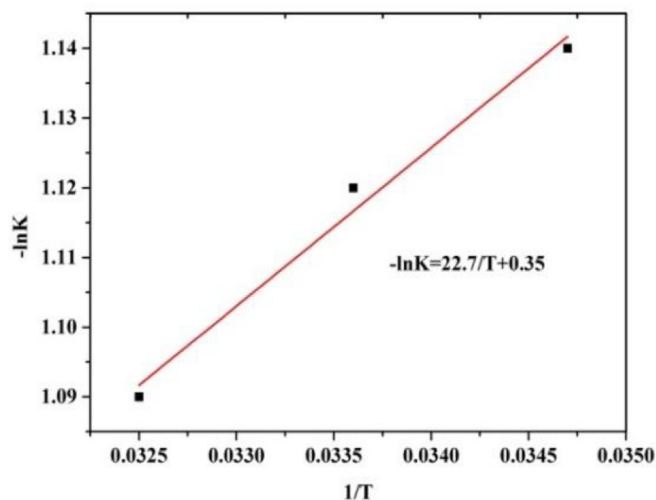


Fig. 21. Relationship between rate constant and temperature in photocatalytic degradation.

solution after irradiation with simulated solar light for 7 h, showing rapid destruction of the pesticides to harmless inorganic materials by this system.

### 3.6. Photocatalytic decomposition kinetics

The degradation was monitored by spectrophotometer using the phosphomolybdate blue method. The overall photocatalytic degradation of dimethoate is represented as

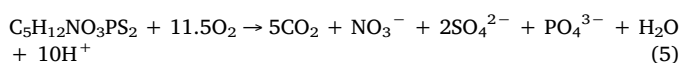


Fig. 20 shows the effects of reaction temperature on the photocatalytic degradation rate; the rate increased with increasing temperature, but the change was small.

The photocatalytic reaction kinetics was investigated using the Langmuir–Hinshelwood kinetic equation. When the dimethoate concentration was very low, the kinetic equation can be expressed as  $\ln(C_0/C_t)K_t + B$ , where  $C_0$  is initial concentration;  $C_t$  is concentration of internal time;  $K_t$  is reaction rate constant [24–26].

Based on the Arrhenius equation,  $\ln k = -E_a/(RT) + B$ , where  $k$  is the rate constant,  $R$  is the molar gas constant,  $T$  is the thermodynamic temperature,  $E_a$  is the apparent activation energy,  $A$  is the pre-exponential factor [38,39]. The relationship between the photocatalytic reaction rate constant and temperature was obtained by plotting  $-\ln k$  as the ordinate and  $1/T$  as the abscissa, as shown in Table 3 and Fig. 21. The linear correlation between  $\ln(C_0/C_t)$  and  $t$  shows that the photocatalytic degradation of dimethoate is first order. The slope,  $E_a/R$ , is 22.7. The calculated activation energy  $E_a$  is 1.9 kJ/mol. The activation

energy of the photocatalytic degradation of dimethoate is low, and is unaffected by the temperature.

Based on the kinetics of the formation and disappearance of major byproducts, we propose that the photocatalytic decomposition of dimethoate occurs via rapid hydroxylation of the methyl groups on oxygen bonded to phosphorus and through C–N cleavage of the amide bond, producing a phosphonic acid molecule, methylamine, formic acid, and mineral ions such as  $\text{SO}_4^{2-}$ ,  $\text{NO}_2^-$ , and  $\text{NO}_3^-$ . Continued attack on the organic compounds eventually results in formation of  $\text{CO}_2$  and mineral ions.

A comparison of the results of our present work with those of some previously reported studies is shown in Table 4. Because the photocatalytic decomposition of dimethoate using  $\text{TiO}_2/\text{SBA-15}$  under sunlight has not yet been achieved, we can only list results for the photocatalytic decomposition of dimethoate using  $\text{TiO}_2/\text{SBA-15}$  under other light sources. The comparison clearly shows that the photocatalytic reaction described here is faster and more efficient than those using most other photocatalysts. Our photocatalyst gives a short photo-degradation time, and is obtained using a low-cost facile synthetic protocol.

## 4. Conclusion

$\text{TiO}_2/\text{SBA-15}$  photocatalysts with highly ordered 2D hexagonal structures were prepared using inorganic  $\text{TiOSO}_4$  obtained from ilmenite as a titanium source by post-synthesis hydrolysis. The effects of different  $\text{TiO}_2$  loadings on the pore structure and morphology were investigated. The results show that most of the  $\text{TiO}_2$  particles were not loaded in the ordered channels of the silica mesoporous molecular sieves, and the porous structure was stable. The  $\text{TiO}_2$  particles loaded over SBA-15 showed significant photocatalytic activity in dimethoate degradation under simulated solar light. The effect of the amount of  $\text{TiO}_2$  loaded on the  $\text{TiO}_2/\text{SBA-15}$  catalysts on the photocatalytic decomposition of dimethoate was investigated. The 26%  $\text{TiO}_2/\text{SBA-15}$  catalyst, with a large specific surface area of  $386 \text{ m}^2/\text{g}$ , showed the highest photocatalytic activity, and dimethoate was completely degraded within 7 h. Recycling tests showed that the catalyst was highly stable, without noticeable activity loss during at least four cycles. The kinetic results show that the photocatalytic degradation of dimethoate is first order. GC-MS showed that the main intermediates generated during photocatalysis were dimethoate, omethoate, *N*-methyl-2-sulfanylacetamide, and *O,O,S*-trimethyl thiophosphorothioate. Accordingly, the  $\text{TiO}_2/\text{SBA-15}$  catalysts prepared in this study are simple to synthesize, and suitable for dimethoate degradation in water because they are easy to separate and reuse. These catalysts avoid the shortcomings of pure  $\text{TiO}_2$  nanopowders, which are easily lost and difficult to recycle. The large surface area of the catalyst enhances dimethoate adsorption and improves the photocatalytic efficiency.

Table 4

Recently reported catalytic systems for dimethoate removal with different catalysts under.

Catalyst	Dimethoate concentration	Degradation time	Photocatalytic activity	Oxidant	Light source	References
P25 (anatase + rutile)	10 mg/L	120min	100%	$\text{H}_2\text{O}_2$	UV	[37]
ZnO	10 mg/L	3 h	95%	$\text{K}_2\text{S}_2\text{O}_8$	UV	[37]
Nano- $\text{TiO}_2$ (anatase + rutile)	$0.39 \times 10^{-4} \text{ mol/L}$	160min	96.82%	$\text{H}_2\text{O}_2/\text{K}_2\text{S}_2\text{O}_8$	UV	[12]
$\text{TiO}_2$ (anatase,sol-gel)/silica gel	0.1 mmol/L	60min	100%	–	UV	[38]
20% $\text{TiO}_2$ /silica gel	200 mg/L	2 h	79.6%	–	UV	[40]
Nano- $\text{TiO}_2$ (anatase + rutile)	$1.96 \times 10^{-4} \text{ mol/L}$	60min	78.88%	$\text{CH}_3\text{COCH}_3 + \text{inorganic cations}$	UV	[36]
P25 + $\text{FeSO}_4$	50 mg/L	450min	80%	$\text{H}_2\text{O}_2$	Solar light	[5]
Thiapyrylium salts	50 mg/L	60min	45%	–	Solar light	[6]
P25(anatase + rutile)/polymer film	1000 ppm	180min	100%	–	UV	[21]
$\text{TiO}_2$ (anatase, ilmenite)/SBA-15	30 ppm	7 h	100%	$\text{H}_2\text{O}_2$	Solar light	Present work

## Acknowledgements

The authors gratefully acknowledge support by the National High Technology Research and Development Program (“863”program) of China (2012AA06A115) and China Postdoctoral Science Foundation (2017M610723).

## Appendix A. Supplementary data

Supplementary data related to this article can be found at <http://dx.doi.org/10.1016/j.dyepig.2018.03.058>.

## References

- [1] Ajmal A, Majeed I, Malik RN, Idriss H, Nadeem MA. Principles and mechanisms of photocatalytic dye degradation on TiO<sub>2</sub> based photocatalysts: a comparative overview. *RSC Adv* 2014;4:37003–26.
- [2] Reddy P, Kim K. A review of photochemical approaches for the treatment of a wide range of pesticides. *J Hazard Mater* 2015;285:325–35.
- [3] Zhang YQ, Zhu J. Composite photocatalytic membrane prepared by embedding porous SiO<sub>2</sub> shell/void/TiO<sub>2</sub> core particles into polycarbonate for photodegrading and removing pollutant from water. *Chem Eng Sci* 2015;126:390–8.
- [4] Liu S, Lim M, Amal R. TiO<sub>2</sub>-coated natural zeolite: rapid humic acid adsorption and effective photocatalytic regeneration. *Chem Eng Sci* 2014;105:46–52.
- [5] Oller I, Gernjak W, Maldonado MI, Perez-Estrada LA, Sanchez-Perez JA, Malato S. Solar photocatalytic degradation of some hazardous water-soluble pesticides at pilot-plant scale. *J Hazard Mater* 2006;138:507–17.
- [6] Gomis J, Arques A, Amat AM, Marin ML, Miranda MA. A mechanistic study on photocatalysis by thiapyrylium salts. Photodegradation of dimethoate, alachlor and pyrimethanil under simulated sunlight. *Appl Catal B: Environ* 2012;123–124:208–13.
- [7] Dong HR, Zeng GM, Tang L, Fan CZ, Zhang C, He XX, He Y. An overview on limitations of TiO<sub>2</sub>-based particles for photocatalytic degradation of organic pollutants and the corresponding countermeasures. *Water Res* 2015;79:128–46.
- [8] Nakata K, Fujishima A. TiO<sub>2</sub> photocatalysis: design and applications. *J Photochem Photobiol C* 2012;13:169–89.
- [9] Mori K, Maki K, Kawasaki S, Yuan S, Yamashita H. Hydrothermal synthesis of TiO<sub>2</sub> photocatalysts in the presence of NH<sub>4</sub>F and their application for degradation of organic compounds. *Chem Eng Sci* 2008;63:5066–70.
- [10] Strauss M, Pastorello M, Sigoli F, Silva J, Mazali I. Singular effect of crystallite size on the charge carrier generation and photocatalytic activity of nano-TiO<sub>2</sub>. *Appl Surf Sci* 2014;319:151–7.
- [11] Boxi SS, Paria S. Visible light induced enhanced photocatalytic degradation of organic pollutants in aqueous media using Ag doped hollow TiO<sub>2</sub> nanospheres. *RSC Adv* 2015;5:37657–68.
- [12] Chen JQ, Wang D, Zhu MX, Gao CJ. Photocatalytic degradation of dimethoate using nanosized TiO<sub>2</sub> powder. *Desalination* 2007;207:87–94.
- [13] Zhang J, Wu WC, Yan S, Chu G, Zhao SL, Wang X, Li C. Enhanced photocatalytic activity for the degradation of rhodamine B by TiO<sub>2</sub> modified with Gd<sub>2</sub>O<sub>3</sub> calcined at high temperature. *Appl Surf Sci* 2015;344:249–56.
- [14] Hu C, Hu XX, Wang LS, Qu JH, Wang AM. Visible-light-induced photocatalytic degradation of azodyes in aqueous AgI/TiO<sub>2</sub> dispersion. *Environ Sci Technol* 2006;40:7903–7.
- [15] Jiang DL, Zhang SQ, Zhao HJ. Photocatalytic degradation characteristics of different organic compounds at TiO<sub>2</sub> nanoporous film electrodes with mixed anatase/rutile phases. *Environ Sci Technol* 2007;41:303–8.
- [16] Chen SY, Zhang YK, Han WL, Wellburn D, Liang J, Liu CS. Synthesis and magnetic properties of Fe<sub>2</sub>O<sub>3</sub>-TiO<sub>2</sub> nano-composite particles using pulsed laser gas phase evaporation-liquid phase collecting method. *Appl Surf Sci* 2013;283:422–9.
- [17] Khan M, Cao WB. Preparation of Y-doped TiO<sub>2</sub> by hydrothermal method and investigation of its visible light photocatalytic activity by the degradation of methylene blue. *J Mol Catal Chem* 2013;376:71–7.
- [18] Choi Y, Koo MS, Bokare AD, Kim D, Bahnemann DW, Choi W. Sequential process combination of photocatalytic oxidation and dark reduction for the removal of organic pollutants and Cr(VI) using Ag/TiO<sub>2</sub>. *Environ Sci Technol* 2017;51:3973–81.
- [19] Nagarjuna R, Roy S, Ganesan R. Polymerizable sol-gel precursor mediated synthesis of TiO<sub>2</sub> supported zeolite-4A and its photodegradation of methylene blue. *Microporous Mesoporous Mater* 2015;211:1–8.
- [20] Kang I, Zhang Q, Yin S, Sato T, Saito F. Improvement in photocatalytic activity of TiO<sub>2</sub> under visible irradiation through addition of N-TiO<sub>2</sub>. *Environ Sci Technol* 2008;42:3622–6.
- [21] Priya DN, Modak JM, Trebše P, Žabar R, Raichura AM. Photocatalytic degradation of dimethoate using LbL fabricated TiO<sub>2</sub>/polymer hybrid films. *J Hazard Mater* 2011;195:214–22.
- [22] Hao C, Li J, Zhang Z, Ji Y, Zhan H. Enhancement of photocatalytic properties of TiO<sub>2</sub> nanoparticles doped with CeO<sub>2</sub> and supported on SiO<sub>2</sub> for phenol degradation. *Appl Surf Sci* 2015;331:17–26.
- [23] Hussain M, Akhter P, Saracco G, Russo N. Nanostructured TiO<sub>2</sub>/KIT-6 catalysts for improved photocatalytic reduction of CO<sub>2</sub> to tunable energy products. *Appl Catal B: Environ* 2015;170–171:53–65.
- [24] Huang HB, Liu GY, Zhan YJ, Xu Y, Lu HX, Huang HL, Feng QY, Wu MY. Photocatalytic oxidation of gaseous benzene under VUV irradiation over TiO<sub>2</sub>/Zeolites catalysts. *Catal Today* 2017;281:649–55.
- [25] Liu C, Lin X, Li YJ, Xu P, Li M, Chen FT. Enhanced photocatalytic performance of mesoporous TiO<sub>2</sub> coated SBA-15 nanocomposites fabricated through a novel approach: supercritical deposition aided by liquid-crystal template. *Mater Res Bull* 2016;75:25–34.
- [26] Wang XJ, Li FT, Hao YJ, Liu SJ, Yang ML. TiO<sub>2</sub>/SBA-15 composites prepared using H<sub>2</sub>TiO<sub>3</sub> by hydrothermal method and its photocatalytic activity. *Mater Lett* 2013;99:38–41.
- [27] Zhao S, Su D, Che J, Jiang BY, Orlov A. Photocatalytic properties of TiO<sub>2</sub> supported on SBA-15 mesoporous materials with large pores and short channels. *Mater Lett* 2011;65:3354–7.
- [28] Perathoner S, Lanzafame P, Passalacqua R, Centi G, Schlögl R, Su DS. Use of mesoporous SBA-15 for nanostructuring titania for photocatalytic applications. *Microporous Mesoporous Mater* 2006;90:347–61.
- [29] Wang W, Song M. Photocatalytic activity of titania-containing mesoporous SBA-15 silica. *Microporous Mesoporous Mater* 2006;96:255–61.
- [30] Sharma MVP, Kumari VD, Subrahmanyam M. TiO<sub>2</sub> supported over SBA-15: an efficient photocatalyst for the pesticide degradation using solar light. *Chemosphere* 2008;73:1562–9.
- [31] Tseng HH, Lee WW, Wei MC, Huang BS, Hsieh MC, Cheng PY. Synthesis of TiO<sub>2</sub>/SBA-15 photocatalyst for the azo dye decolorization through the polyol method. *Chem Eng J* 2012;210:529–38.
- [32] Yang J, Zhang J, Zhu LW, Chen SY, Zhang YM, Tang Y, Zhu YL, Li YW. Synthesis of nano titania particles embedded in mesoporous SBA-15: characterization and photocatalytic activity. *J Hazard Mater* 2006;137:952–8.
- [33] Suraja PV, Yaakob Z, Binitha NN, Resmi MR, Siliya PP. Photocatalytic degradation of dye pollutant over Ti and Co doped SBA-15: comparison of activities under visible light. *Chem Eng J* 2011;176–177:265–71.
- [34] Acosta-Silva YJ, Nava R, Hernández-Morales V, Macías-Sánchez SA, Gómez-Herrera ML, Pawelec B. Methylene blue photodegradation over titania-decorated SBA-15. *Appl Catal B: Environ* 2011;110:108–17.
- [35] Li ZH, Wang ZC, Li G. Preparation of nano-titanium dioxide from ilmenite using sulfuric acid-decomposition by liquid phase method. *Powder Technol* 2016;287:256–63.
- [36] Chen JQ, Hu ZJ, Wang D, Gao CJ, Ji R. Photocatalytic mineralization of dimethoate in aqueous solutions using TiO<sub>2</sub>: parameters and by-products analysis. *Desalination* 2010;258:28–33.
- [37] Evgenidou E, Konstantinou I, Fytianos K, Albanis T. Study of the removal of dichlorvos and dimethoate in a titanium dioxide mediated photocatalytic process through the examination of intermediates and the reaction mechanism. *J Hazard Mater* 2006;137:1056–64.
- [38] Echavia GRM, Matzuzawa F, Negishi N. Photocatalytic degradation of organophosphate and phosphoglycine pesticides using TiO<sub>2</sub> immobilized on silica gel. *Chemosphere* 2009;76:595–600.
- [39] Arques A, Amat AM, García-Ripoll A, Vicente R. Detoxification and/or increase of the biodegradability of aqueous solutions of dimethoate by means of solar photocatalysis. *J Hazard Mater* 2007;146:447–52.
- [40] Negishi N, Sano T, Hirakawa T, Koiwa F, Chawengkijwanich C, Pimpha N, Echavia GM. Photocatalytic detoxification of aqueous organophosphorus by TiO<sub>2</sub> immobilized silica gel. *Appl Catal B: Environ* 2012;128:105–18.